CHAPTER 3

TRANSFER OF INFORMATION AROUND A CONCAVE CORNER *

*Part of this work has been published as:

Rajan Agrahari, Akhlesh Lakhtakia, and Pradip Kumar Jain, "Towards information transfer around a concave corner by a surface-plasmon-polariton wave," *IEEE Photonics Journal*, vol. 11, no. 1, art. no. 6100112, 2019.

3.1. Overview

Time-domain Maxwell equations are solved using the finite-difference time-domain method to investigate the transfer of information via a pulse-modulated carrier SPP wave around a concave corner formed by two planar metal/air interfaces. The signal is launched along the first metal/air interface and received along the second metal/air interface. The corner angle affects the intensity and the duration of the received signal, but its shape is largely independent of the corner angle of the corner. Accordingly, the signal received around the concave corner is strongly and positively correlated with the transmitted signal, a promising result for SPP wave-based optical interconnects. The energy of the received signal varies with the frequency of the carrier SPP wave. The received signal is better correlated with the transmitted signal when the carrier frequency is higher for a fixed value of the corner angle.

3.2. Introduction

Chapter 2 provides the solution of the Maxwell equations in the time domain to investigate the jump of a pulse-modulated carrier SPP wave across a semi-infinite gap on the metallic side of a planar metal/dielectric interface [Agrahari *et al.* (2018)]. The signal continues to propagate in the forward direction for a long distance after the abrupt termination of the metal, remaining strongly and positively correlated [Rodgers and Nicewander (1988)] with the transmitted signal. When the metal/air interface is restored after a gap of width equal to the carrier wavelength in free space, the signal received across the gap is strongly and positively correlated with the transmitted signal. These are promising results for information transfer through SPP-wave-based optical interconnects.

Not only gaps but concave corners are also common in electronic chips [Wada *et al.* (2002), Vlasov and McNabb (2004)]. The corners need not be right-angled, as is the case covered implicitly in Chapter 2. Accordingly, the current chapter addresses the

initial-boundary-value problem for information transmitted by a pulse-modulated SPP wave when the metal/dielectric interface bends abruptly to form a corner of angle $\alpha < \pi$ as shown in Fig. 3.1.The Drude model is used for the relative permittivity of the metal and the Lorentz model for that of the dielectric material [Kittel (1974)]. The finite-difference time-domain (FDTD) method [Yee (1966), Elsherbeni and Demir (2016)] is used to solve the time-domain Maxwell equations in order to determine the temporal evolution of the electromagnetic field everywhere in the computational domain [Agrahari *et al.* (2018)]. As all calculations are performed in the time domain, constraints imposed by boundary conditions in frequency-domain analyses [Oulton *et al.* (2007), Novitsky (2010), Foley *et al.* (2014), Armin *et al.* (2018)] are completely avoided. The Pearson correlation coefficient [Rodgers and Nicewander (1988)] of the appropriate component of the Poynting vector at two points, one on each of the two metal/dielectric interfaces forming the corner is calculated in order to compare the transmitted and the received signals, with air chosen as the dielectric material.

A brief description of the theoretical treatment is provided in Sec. 3.3, followed by a discussion of the obtained results in Sec. 3.4. The chapter concludes with some closing remarks in Sec. 3.5.

3.3. Theory in Brief

The computational domain of the chosen initial-boundary-value problem is depicted in Fig. 3.1. The relevant physical domain is identified by the region $\Re : \{|x| \leq a, -\infty < y < \infty, -b \leq z \leq c\}$ and the relevant temporal domain as $T : \{t \geq 0\}$. Thus, $\Re \times T$ is the computational domain. The blue region $\Re_A$ is occupied by a homogeneous dielectric material labeled A and the ocher region $\Re_B$ by a homogeneous metal labeled B. Both materials are chosen such that an SPP wave can travel guided by

the interface $z = 0$ at a fixed frequency f_c [Maier (2007), Homola (2006), Polo *et al.* (2013)]. The horizontal and the bent metal/dielectric interfaces form a concave corner of angle $\alpha < \pi$. The physical domain $\Re$ is encapsulated by perfectly match layers (PMLs) [Agrahari *et al.* (2018), Berenger (1994)] above the plane $z = c$, below the plane $z = -b$, and to the right of the plane $x = a$ in order to prevent reflection into $\Re$. Even so, the dimensions b and c must be chosen to be sufficiently large that the reflections are minuscule. As material B is a metal, b should exceed the skin depth [Iskander (2013)] at frequency f_c.

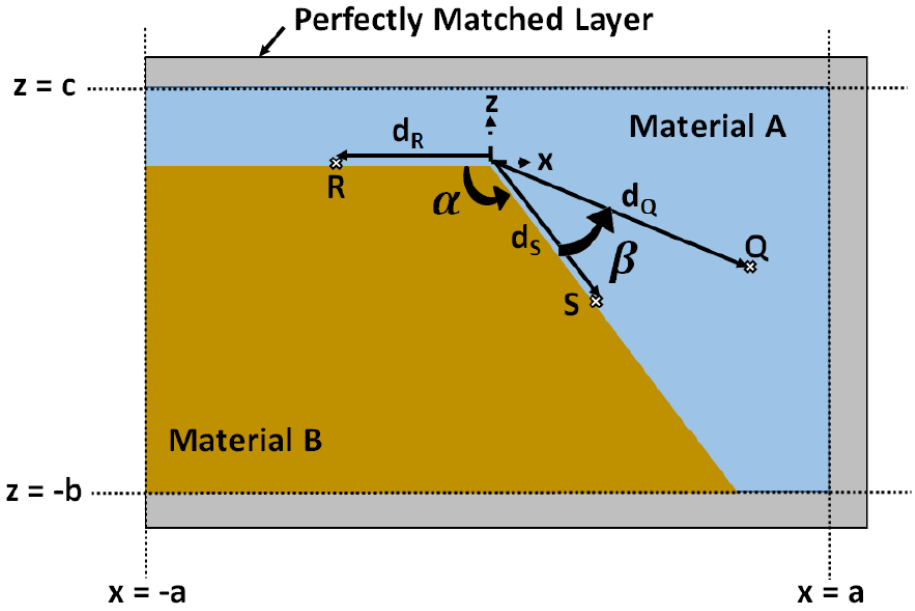

Figure 3.1: Schematic of the computational domain of the initial-boundary-value problem when the metal bends to form a corner of angle $\alpha \in (0, \pi)$. Materials A and B are dielectric and metallic, respectively. The computational domain is bounded by three perfectly matched layers. The point labeled R is identified as the transmission point and the point S as the reception point. Point Q is chosen for analysis of the signal scattered in the region occupied by material A beyond the corner.

In the FDTD simulations, a pulse-modulated SPP wave is launched into the computational domain from the plane $x = -a$ at the time $t = 0$. To analyze the adequacy of information transmission around the corner, (i) a point labeled R $\left(x_R = -d_R,\ z_R = 0^+\right)$

on the horizontal metal/dielectric interface is identified as the point of transmission and (ii) a point labeled S ($x_S = -d_S \cos\alpha$, $z_S = -d_S \sin\alpha$) on the bent metal/dielectric interface is identified as a point of reception, as shown in Fig. 3.1. A point labeled Q ($x_Q = -d_Q \cos(\alpha+\beta)$, $z_Q = -d_Q \sin(\alpha+\beta), \beta > 0$) is chosen in the region $\Re_A$ for analysis of the signal scattered into material A beyond the plane $x = 0$. The dimension a of the computational domain is chosen keeping the propagation distance of the carrier SPP wave in mind. Furthermore, the depths of penetration of the carrier SPP wave in materials A and B have to be considered while deciding the dimensions b and c. All fields in this problem are independent of y. All other computational details are provided in Chapter 2.

3.4. Numerical Results and Discussion

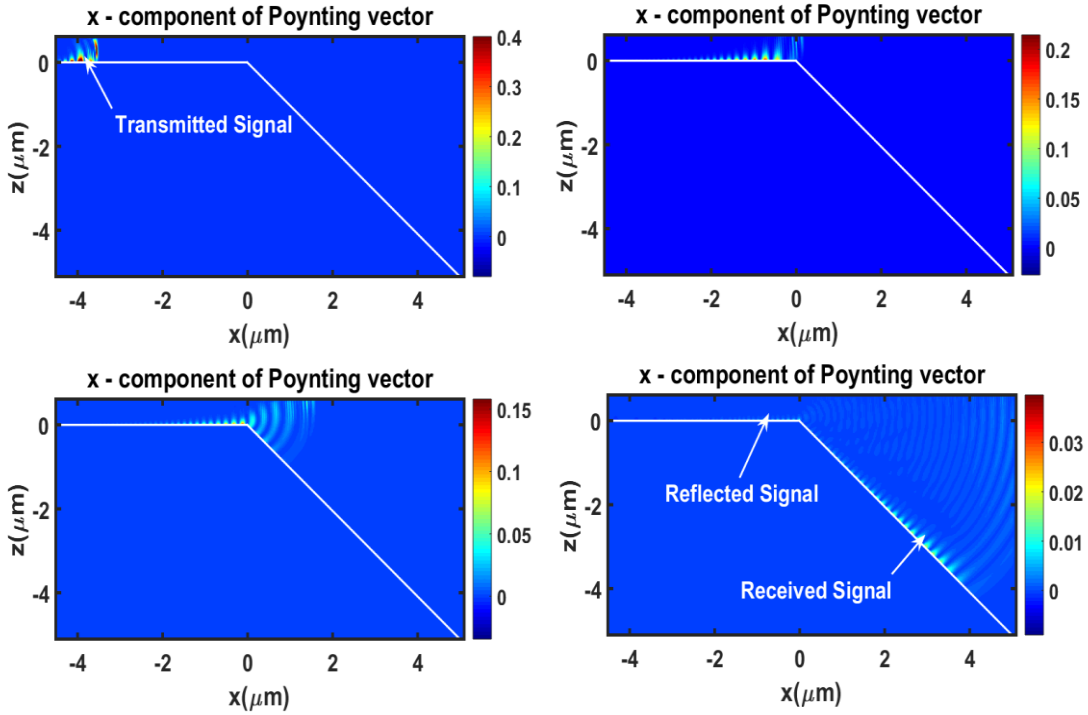

Figure 3.2: Four snapshots of normalized $P_x(x,z,t)$ taken at (top left) $t = 4.94$ fs, (top right) $t = 17.26$ fs, (bottom left) $t = 21.96$ fs and (bottom right) $t = 37.41$ fs, when $\lambda_c = 500$ nm and $\alpha = 135^\circ$. Multiply by 1.1375×10^{-4} W m^{-2} to obtain unnormalized $P_x(x,z,t)$.

For all numerical results presented here, material A is chosen to be air by setting $p_A = 0$

in Eq. (2.4) and material B is chosen to be bulk silver with $\omega_B = 1.352 \times 10^{16}$ rad s^{-1} and $\tau_B = 17 \times 10^{-15}$ s for use in Eq. (2.6) [Yang *et al.* (2015)]. FDTD simulations are undertaken with the following parameters: $a = 5000$ nm, $b = 5000$ nm, $\Delta x = \Delta z = 10$ nm, and $\Delta t = 0.022$ fs. Furthermore, $c \in \{318, 524, 775, 1073\}$ nm for $\lambda_c \in \{400, 500, 600, 700\}$ nm, where the free-space wavelength $\lambda_c = 2\pi / k_c$.

The phenomenon under investigation is illustrated by the four snapshots in Fig. 3.2 showing the spatiotemporal variation of the x-directed component of the instantaneous Poynting vector

$$\mathbf{P}(x, z, t) = \mathbf{E}(x, z, t) \times \mathbf{H}(x, z, t) \tag{3.1}$$

for $\lambda_c = 500$ nm and $\alpha = 135^\circ$. The pulse-modulated carrier SPP wave is launched at $t = 0$ from the plane $x = -a$. The snapshots of $P_x(x, z, t) = \hat{\mathbf{u}}_x \bullet \mathbf{P}(x, z, t)$ are taken at $t \in \{4.94, 17.26, 21.96, 37.41\}$ fs. The transmitted signal can be clearly seen in the first snapshot ($t = 4.94$ fs). Arriving in the vicinity of the plane $x = 0$, the signal encounters the concave corner of angle α, as depicted in the second snapshot ($t = 17.26$ fs). As a result, the signal is: (i) partly reflected along the horizontal metal/dielectric interface, (ii) partly guided along the bent metal/dielectric interface, and (iii) partly scattered into the region $\Re_A$ to the right of the plane $x = 0$, as shown in the third and the fourth snapshots ($t = 21.96$ and 37.41 fs). All plots of the components of the instantaneous Poynting vector in this chapter are normalized with respect to the magnitude 1.1375×10^{-4} W m^{-2}. This normalization factor is obtained by integrating $P_x(-a^+, 0^+, t)$ with respect to t from 0 to 70 fs when $\lambda_c = 500$ nm, and then dividing the result by the duration for which $P_x(-a^+, 0^+, t)$ is at least 50% of its peak value.

3.4.1. Effect of Corner Angle on Information Transmission

With a view to ascertaining the effect of the corner angle α on the signal received at S, the carrier wavelength $\lambda_c = 500$ nm is fixed and the angle α is varied from 75° to 180°. Temporal profile of the component

$$P_{ax}(x_R, z_R, t) = \hat{\mathbf{u}}_z \bullet \mathbf{P}(x_R, z_R, t) \tag{3.2}$$

of the Poynting vector at the transmission point R on the horizontal metal/dielectric interface are shown in Fig. 3.3 for $\alpha = 135^\circ$ when $d_R = 8\lambda_c$. The left panel of the figure shows $P_{ax}(x_R, z_R, t)$ for $t \in [0, 33]$ fs and the right panel for $t \in [33, 70]$ fs. The transmitted signal at point R is evident for $t \in [3.3, 15.4]$ fs, and the reflected signal at the same point begins to appear at $t \simeq 34$ fs. The intensity of the reflected signal is very weak, almost in the noise level when compared with the transmitted signal, which indicates that most of the energy of the transmitted signal is scattered by the concave corner with some of it possibly propagating guided by the bent metal/dielectric interface.

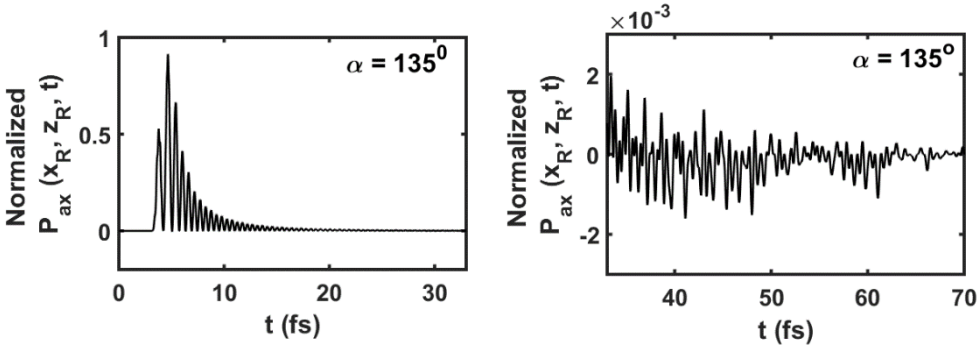

Figure 3.3: Temporal profile of normalized $P_{ax}(x_R, z_R, t)$ when $d_R = 8\lambda_c$, $\lambda_c = 500$ nm, and $\alpha = 135^\circ$. The transmitted signal (left) and the reflected signal (right) at point R are sufficiently separated from each other in time to be distinctly identified. Multiply by 1.1375×10^{-4} W m^{-2} to obtain unnormalized $P_{ax}(x_R, z_R, t)$.

The dependence of the reflected signal at point R on the corner angle α can be gleaned from the plots of $P_{ax}(x_R, z_R, t)$ vs. $t \in [33, 70]$ fs for $d_R = 8\lambda_c$ and

$\alpha \in \{75^\circ, 90^\circ, 120^\circ, 135^\circ, 150^\circ, 180^\circ\}$ in Fig. 3.4. Even though the reflected signal in Fig. 3.4 is significantly weaker than the transmitted signal (shown in the left panel of Fig. 3.3) regardless of the value of α, the reflected signal is definitely stronger when α is acute than when α is obtuse. As α increases, the reflected signal weakens. Since there is no discontinuity at $\{x = 0,\ z = 0\}$ when $\alpha = 180^\circ$, zero reflection must occur; indeed, that is borne out by the absence of negative values of P_{ax} in the bottom right panel of Fig. 3.4. Therefore, the vast majority of the transmitted signal is either scattered in material A (air) or is propagated along the bent metal/dielectric interface, when $\alpha < 180^\circ$.

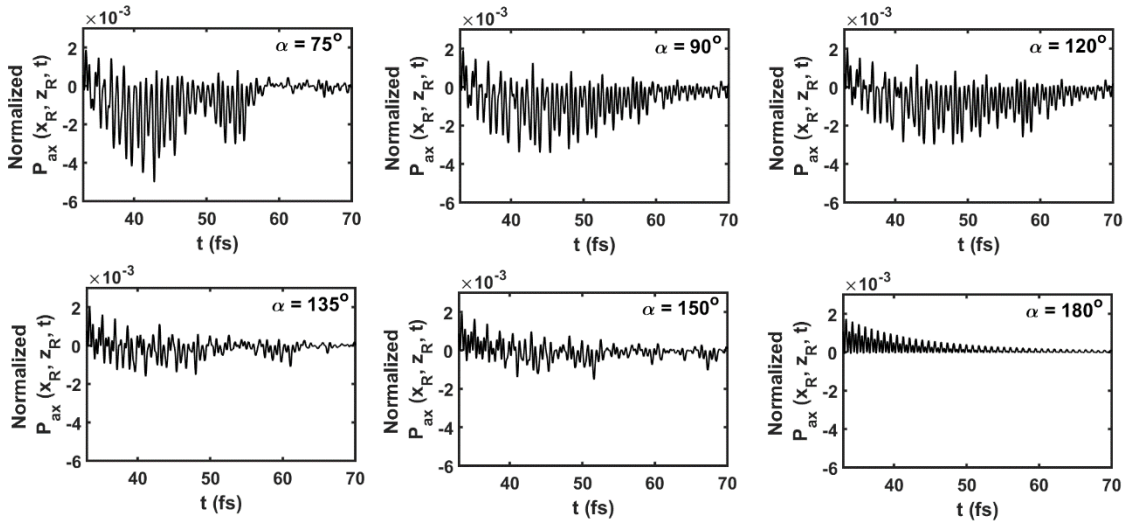

Figure 3.4: Temporal profile of normalized $P_{ax}(x_R, z_R, t)$ when $d_R = 8\lambda_c$, $\lambda_c = 500$ nm, and $\alpha \in \{75^\circ, 90^\circ, 120^\circ, 135^\circ, 150^\circ, 180^\circ\}$. Each profile is of the reflected signal at point R. Multiply by 1.1375×10^{-4} W m^{-2} to obtain unnormalized $P_{ax}(x_R, z_R, t)$.

The signal received at the reception point S also depends on the corner angle α. The temporal profile of the axial component of the Poynting vector

$$P_{ax}(x_S,\ z_S,\ t) = -\left(\hat{\mathbf{u}}_x \cos\alpha + \hat{\mathbf{u}}_z \sin\alpha\right) \bullet \mathbf{P}(x_S,\ z_S,\ t) \tag{3.3}$$

at point S on the bent metal/dielectric interface is shown in Fig. 3.5 for $d_S = 5\lambda_c$ and $\alpha \in \{75^\circ, 90^\circ, 120^\circ, 135^\circ, 150^\circ, 180^\circ\}$. The intensity of the received signal is low for

$\alpha = 75^\circ$, but it increases monotonically as α increases to 180°. This increase is consistent with the decrease of the intensity of the reflected signal at R in Fig. 3.4. However, since the reflected signal is weak for all values of α in Fig. 3.4, the energy of the signal scattered in $\Re_A$ beyond the plane $x = 0$ must decrease as α increases, in accordance with the principle of conservation of energy.

For all values of α in Fig. 3.5, the shape of the received pulse is approximately the same as that of the transmitted pulse at R (shown in the left panel of Fig. 3.3). No appreciable precursor has developed because the launching plane $x = -a$ is quite close to the corner. When the value of a is considerably higher, a precursor does develop (although not shown here). Nevertheless, the received signal is distorted in comparison to the transmitted signal.

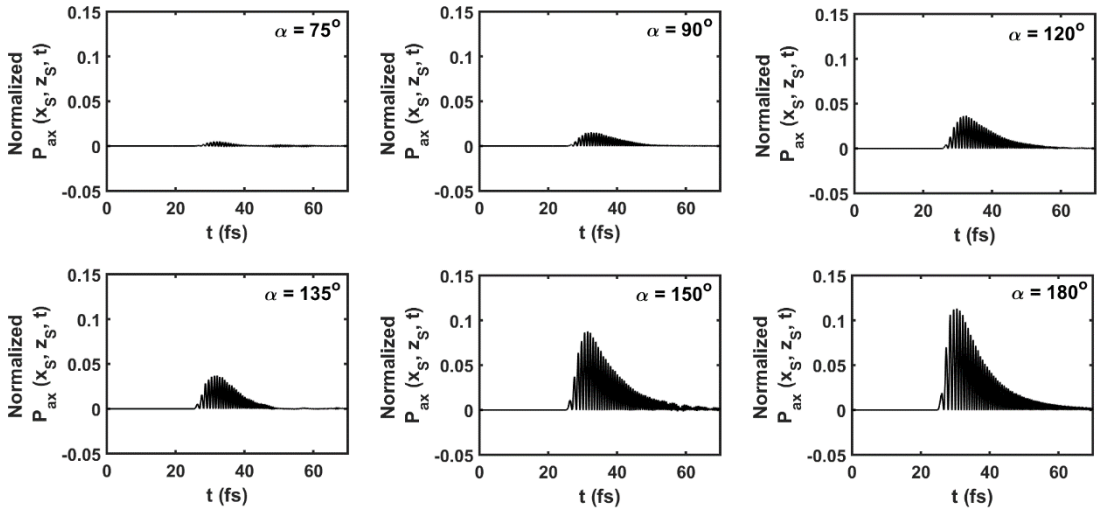

Figure 3.5: Temporal profile of normalized $P_{ax}(x_S, z_S, t)$ when $d_S = 5\lambda_c$, $\lambda_c = 500$ nm, and $\alpha \in \{75^\circ, 90^\circ, 120^\circ, 135^\circ, 150^\circ, 180^\circ\}$. Each profile is of the received signal at point S. Multiply by 1.1375×10^{-4} W m^{-2} to obtain unnormalized $P_{ax}(x_S, z_S, t)$.

If the duration of the received signal is quantified as the time interval for which $P_{ax}(x_S, z_S, t)$ exceeds 50% of its peak value, the received signal's duration is $\{7.91, 11.65, 10.50, 10.41, 10.30, 10.10\}$ fs for $\alpha \in \{75^\circ, 90^\circ, 120^\circ, 135^\circ, 150^\circ, 180^\circ\}$.

The signal duration at S is approximately constant at 10.3 fs when α is obtuse but decreases when α is acute. The analogously defined duration of the transmitted signal in the left panel of Fig. 3.3 is 2.3 fs. The increasing signal duration at the reception point S compared to that of the signal transmitted at point R indicates that the pulse broadens as it propagates on the metal/air interface. This observation is consistent with different spectral components of the transmitted signal having different phase speeds, as discussed in Chapter 2.

A comparison of the left panel of Fig. 3.3 with the bottom right panel of Fig. 3.5 shows that the energy of the signal weakens as it travels along a planar metal/dielectric interface, in agreement with Chapter 2, because of attenuation of the carrier SPP wave [Polo *et al.* (2013)] due to the metal being dissipative [Johnson and Christy (1972)].

In order to quantify the similarity of the signal received at point S to the signal transmitted at point R, the Pearson correlation coefficient $\rho_{RS} \in [-1, 1]$ [Rodgers and Nicewander (1988)] between the received and the transmitted signals is determined. This coefficient is defined as

$$\rho_{RS} = \frac{\sum_{\ell=1}^{N} \left[\Delta P_{ax}(x_R, z_R, t_\ell) \cdot \Delta P_{ax}(x_S, z_S, t_\ell - \bar{t}) \right]}{\sqrt{\left\{ \sum_{\ell=1}^{N} \left[\Delta P_{ax}(x_R, z_R, t_\ell) \right]^2 \right\}} \cdot \sqrt{\left\{ \sum_{\ell=1}^{N} \left[\Delta P_{ax}(x_S, z_S, t_\ell - \bar{t}) \right]^2 \right\}}}, \tag{3.4}$$

where

$$\Delta P_{ax}(x, z, t_\ell) = P_{ax}(x, z, t_\ell) - \frac{1}{N} \sum_{\kappa=1}^{N} P_{ax}(x, z, t_\kappa) \quad \ell \in [1, N], \tag{3.5}$$

and $\bar{t}$ is the time of flight of a plane wave in vacuum across the distance between the points of transmission and reception.

The Pearson correlation coefficient correlates the shapes of the transmitted and received signals, with positive values indicating correlation and negative values

indicating a lack of correlation. The closer that $|\rho_{RS}|$ is to unity, the stronger is the correlation or anticorrelation, as indicated by the sign of ρ_{RS}. If the received signal is independent of the transmitted signal, then $\rho_{RS} = 0$. Thus, the Pearson correlation coefficient is a simple, but not comprehensive, measure of the fidelity of information transfer.

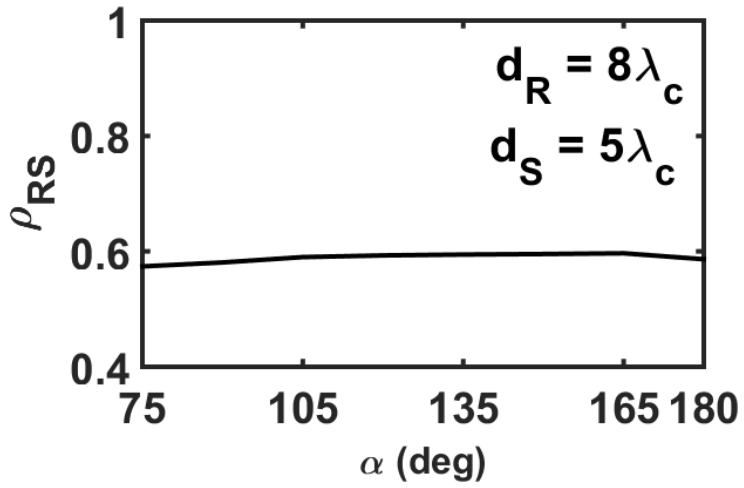

Figure 3.6: Pearson correlation coefficient ρ_{RS} between $P_{ax}(x_R, z_R, t)$ and $P_{ax}(x_S, z_S, t)$ as a function of $\alpha \in [75^\circ, 180^\circ]$ when $d_R = 8\lambda_c$, $d_S = 5\lambda_c$, and $\lambda_c = 500$ nm.

Figure 3.6 shows the variation of ρ_{RS} with $\alpha \in [75^\circ, 180^\circ]$ when $d_R = 8\lambda_c$ and $d_S = 5\lambda_c$. Since the shape of the received signal is approximately the same as that of the transmitted signal, as indicated by Figs. 3.3 and 3.5, $\rho_{RS} = 0.585 \pm 0.015$ over the chosen range of α, thereby confirming that the shape of the signal received at S is largely independent of the corner angle of the corner. However, ρ_{RS} does not have higher values since the duration of the received signal is different from that of the transmitted signal. The high and positive values of ρ_{RS} also indicate that information can indeed be transferred by a carrier SPP wave around a concave corner.

3.4.2. Effect of Carrier Wavelength on Information Transmission

In order to study the effect of the carrier wavelength λ_c on information transfer, Eq. (3.15) is used to plot the dispersion diagram in Fig. 3.7 for an SPP wave guided by the silver/air interface. The phase speed $\omega_c / \mathrm{Re}(q_c)$ is higher but the attenuation rate $\mathrm{Im}(q_c)$ is lower for larger λ_c.

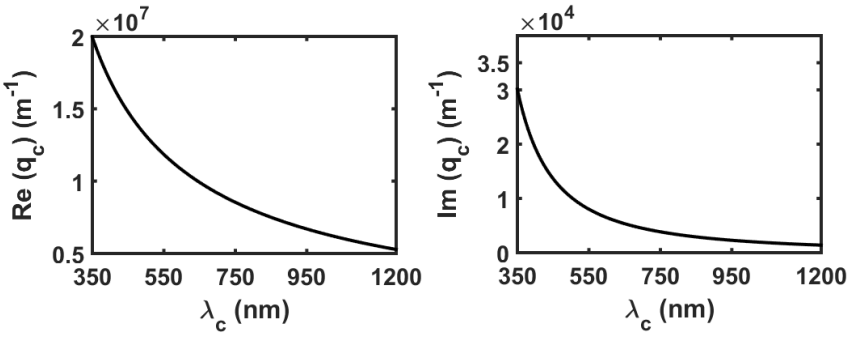

Figure 3.7: Real and imaginary parts of the SPP wavenumber q_c as a function of carrier wavelength λ_c.

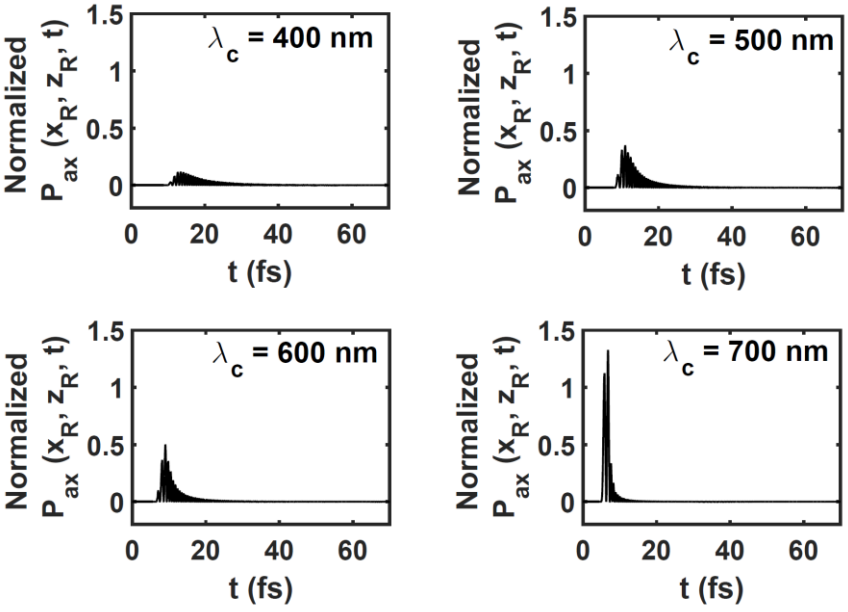

Figure 3.8: Temporal profile of normalized $P_{ax}(x_R, z_R, t)$ when $d_R = 5\lambda_c$, $\lambda_c \in \{400, 500, 600, 700\}$ nm, and $\alpha = 135^\circ$. Each profile is of the transmitted signal at point R. Multiply by 1.1375×10^{-4} W m^{-2} to obtain unnormalized $P_{ax}(x_R, z_R, t)$.

Next, $\alpha = 135^\circ$ was fixed but $\lambda_c \in \{400, 500, 600, 700\}$ nm was varied. The

temporal profiles of $P_{ax}(x_R, z_R, t)$ at the transmission point R are shown in Fig. 3.8 when $d_R = 5\lambda_c$. The peak intensity of the transmitted signal at point R increases as λ_c increases. Figure 3.9 shows the corresponding temporal profiles of $P_{ax}(x_S, z_S, t)$ (at the reception point S) calculated with $d_S = 5\lambda_c$. A comparison of the four profiles in this figure indicates that the peak intensity of the received signal increases as λ_c increases, in part because of the higher peak of the transmitted signal (Fig. 3.8), and in part because the attenuation rate of the carrier SPP wave decreases as λ_c increases [Agrahari *et al.* (2018)].

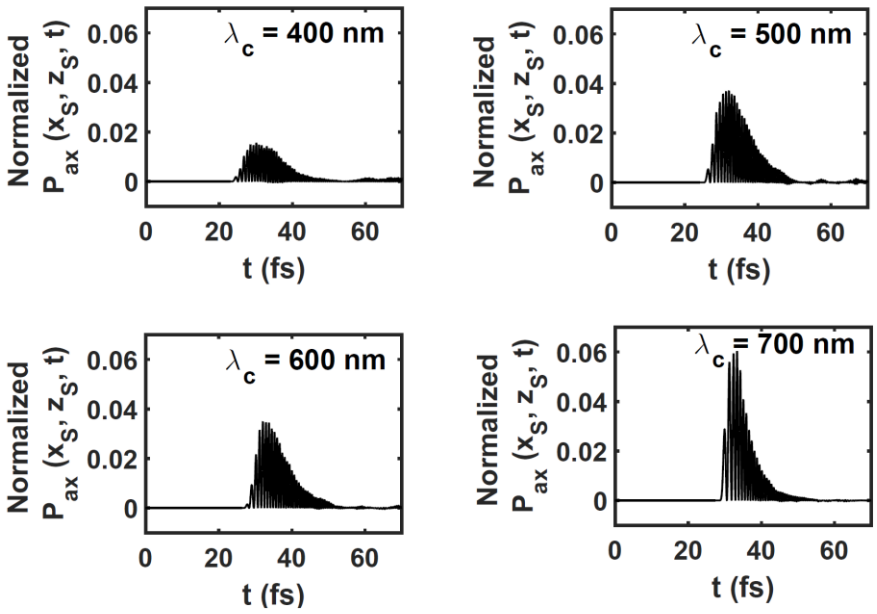

Figure 3.9: Temporal profile of normalized $P_{ax}(x_S, z_S, t)$ when $d_R = 5\lambda_c$, $d_S = 5\lambda_c$, $\lambda_c \in \{400, 500, 600, 700\}$ nm, and $\alpha = 135^\circ$. Each profile is of the received signal at point S. Multiply by 1.1375×10^{-4} W m^{-2} to obtain unnormalized $P_{ax}(x_S, z_S, t)$.

Furthermore, the shape of the received signal at point S is about the same as that of the transmitted signal at point R, although pulse broadening occurs for every $\lambda_c \in \{400, 500, 600, 700\}$ nm. However, the transmitted signal's duration at point R and the received signal's duration at point S are, markedly lower for $\lambda_c = 700$ nm than for the other three values of λ_c. Quantified as the time interval for which P_{ax} exceeds 50% of its

peak value, the duration of the transmitted signal in Fig. 3.8 is $\{6.49, 3.90, 2.59, 1.50\}$ fs for $\lambda_c \in \{400, 500, 600, 700\}$ nm. Correspondingly, the duration of the received signal in Fig. 3.9 is $\{11.53, 10.41, 9.31, 5.68\}$ fs. Thus, pulse broadening continues to occur on the metal/air interface after the signal has gone around the concave corner.

Table 3.1 shows the variation of ρ_{RS} with λ_c for $d_R = 5\lambda_c$ and $d_S = 5\lambda_c$, when $\alpha = 135^\circ$. As λ_c increases from 400 to 700 nm, ρ_{RS} reduces from 0.76 to 0.67. Thus the received signal is better correlated with the transmitted signal when the carrier wavelength λ_c is lower.

Thus, the energy content of the received signal increases but the shape and duration of the received signal differ more from those of the transmitted signal, as λ_c increases.

Table 3.1: ρ_{RS} in Relation to λ_c When $d_R = 5\lambda_c$, $d_S = 5\lambda_c$, and $\alpha = 135^\circ$

Carrier wavelength λ_c (nm)	**Pearson correlation coefficient** ρ_{RS}
400	0.7642
500	0.7545
600	0.7278
700	0.6683

3.4.3. Scattered Signal

The signal arriving at the concave corner not only travels along the bent metal/dielectric interface but is also scattered into the region $\Re_A$ to the right of the plane $x = 0$. In order to determine the dependency of the scattered field on the radial distance from the corner $\{x = 0, y = 0\}$, attention is focused on point Q identified in Fig. 3.1 and the radial component

$$P_{rad}(x_Q, z_Q, t) = -\left[\hat{\mathbf{u}}_x \cos(\alpha+\beta) + \hat{\mathbf{u}}_z \sin(\alpha+\beta)\right] \bullet \mathbf{P}(x_Q, z_Q, t) \qquad (3.6)$$

of the instantaneous Poynting vector is computed as a function of the distance d_Q .

With the point Q located far from the corner, $d_Q / \lambda_c \in [3,9]$ is varied for $\lambda_c = 500$ nm. The dependency of the scattered field on the radial distance is determined for two representative cases:

(i). $\alpha = 90^\circ$ and $\beta \in \{0^\circ, 90^\circ\}$ and

(ii). $\alpha = 135^\circ$ and $\beta \in \{0^\circ, 45^\circ\}$

Figure 3.10 presents the peak intensity of the temporal profile of $P_{rad}(x_Q, z_Q, t)$ as a function of d_Q for both cases. In order to facilitate comparison, the peak intensity for each value of β is normalized to unity for $d_Q = 9\lambda_c$. Also plotted is a similarly normalized curve for the $1/d_Q$ dependence.

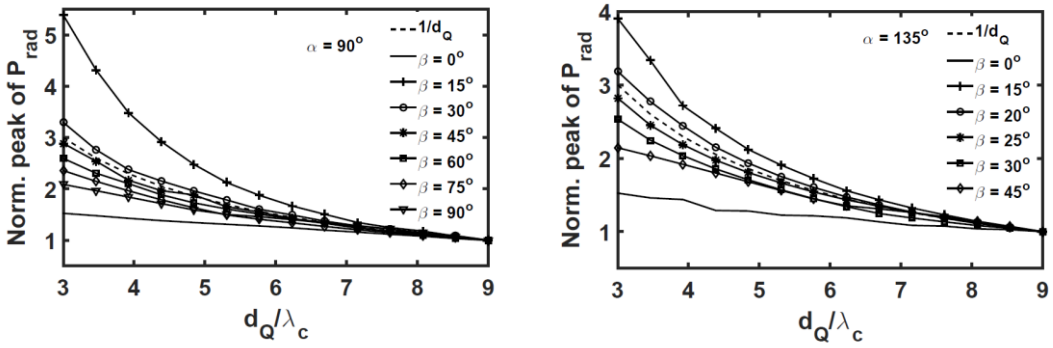

Figure 3.10: Normalized peak intensity of $P_{rad}(x_Q, z_Q, t)$ as a function of $d_Q / \lambda_c \in [3,9]$ with $\lambda_c = 500$ nm fixed. Left: $\alpha = 90^\circ$ and $\beta \in \{0^\circ, 90^\circ\}$. Right: $\alpha = 135^\circ$ and $\beta \in \{0^\circ, 45^\circ\}$. The peak intensity for each value of β is normalized to unity for d_Q / λ_c. The normalized curve for the $1/d_Q$ dependence is also shown.

As d_Q increases, the peak intensity of $P_{rad}(x_Q, z_Q, t)$ decreases as $1/d_Q^{\gamma}$ for every value of β in Fig. 3.10. When $\alpha = 90^\circ$, $\gamma \simeq 1$ for $\beta \in [30^\circ, 90^\circ]$, $\gamma \simeq 1.5$ for $\beta = 15^\circ$, and $\gamma \simeq 0.5$ for $\beta = 0^\circ$ in Fig. 3.10 (left). Similarly, when $\alpha = 135^\circ$, $\gamma \simeq 1$ for $\beta \in [20^\circ, 45^\circ]$,

$\gamma \simeq 1.4$ for $\beta = 15^\circ$, and $\gamma \simeq 0.5$ for $\beta = 0^\circ$ in Fig. 3.10 (right). According to the Huygens principle for two-dimensional frequency-domain electromagnetics, electromagnetic field phasors vary as $1/d_Q^{0.5}$ and the time-averaged Poynting vector as $1/d_Q$ in the far zone [Lakhtakia *et al.* (1989), Chew (1999)]. Thus, proximity to the bent metal/dielectric interface affects the scattered signal in the region R_A beyond the plane $x = 0$.

3.5. Concluding Remarks

The time-domain Maxwell equations are solved using the FDTD method to investigate the transfer of information via a pulse-modulated carrier SPP wave around a concave corner formed by two planar metal/air interfaces. Launched along the first metal/air interface, the signal is partly reflected along the first metal/air interface, partly scattered into air beyond the corner, and partly travels along the second metal/air interface.

The reflected signal is two orders of magnitude weaker in energy than the transmitted signal. The reflected signal weakens as the corner angle α increases and vanishes for $\alpha = 180^\circ$. The energy of the signal scattered into air beyond the corner is inversely proportional to the distance from the corner except in an angular sector close to the second metal/air interface.

The intensity of the received signal at the second metal/air interface increases as either the corner angle α increases and/or the carrier wavelength λ_c increases. However, the duration at a fixed point of reception on the second metal/air interface is approximately constant when α is obtuse but decreases when α is acute. The longer the signal propagates on the second metal/air interface, the larger is its duration. The shape of the received signal is largely independent of the corner angle of the corner and the carrier wavelength. Statistical analysis reveals that the signal after the concave corner is strongly and positively correlated with the transmitted signal, a promising result for SPP-

wave-based optical interconnects. The received signal is better correlated with the transmitted signal when the carrier wavelength is lower for a fixed value of the corner angle.